



Contents lists available at ScienceDirect

Ultramicroscopy

journal homepage: www.elsevier.com/locate/ultramic

Scattering delocalization and radiation damage in STEM-EELS

R.F. Egerton

Physics Department, University of Alberta, Edmonton T6G 2E1, Canada

ARTICLE INFO

Article history:

Received 21 July 2016

Revised 4 February 2017

Accepted 18 February 2017

Available online xxx

Keywords:

TEM

STEM

EELS

Inelastic scattering

Delocalization

Radiation damage

ABSTRACT

We discuss the delocalization of the inelastic scattering of 60–300 keV electrons in a thin specimen, for energy losses below 50 eV where the delocalization length exceeds atomic dimensions. Analytical expressions are derived for the point spread function (PSF) that describes the radial distribution of this scattering, based on its angular distribution and a dielectric representation of energy loss. We also compute a PSF for energy deposition, which is directly related to the radiolysis damage created by a small-diameter probe. These concepts are used to explain the damage kinetics, measured as a function of probe diameter, in various polymers. We also evaluate a “leapfrog” coarse-scanning procedure as a technique for energy-filtered imaging of a beam-sensitive specimen.

© 2017 Elsevier B.V. All rights reserved.

1. Introduction

The purpose of this paper is to develop analytical formulas, based on wave optics and dielectric theory, to describe the spatial extent of inelastic scattering and the resulting energy deposition that leads to radiolysis damage in a beam-sensitive TEM specimen. Measurements indicate that the delocalization distance is a few nm for valence-electron scattering, and tens of nm for dipole-mode vibrational losses, implying that the EELS signal is generated mainly *outside* the electron probe, in the case of the sub-nm probes used for high-resolution STEM. The delocalization formulas will be applied to previous EELS measurement on polymers, to provide an explanation for the apparent reduction in radiation sensitivity with decreasing probe diameter.

Although scattering delocalization limits the spatial resolution of energy-loss spectroscopy and energy-filtered imaging, it can be exploited to minimize radiation damage, as already demonstrated for aloof-beam spectroscopy of vibrational energy losses [1–3]. The aloof mode (electron probe beyond the edge of the specimen) is useful for spectroscopy but it examines limited regions of the specimen (adjacent to the edge) and is largely incapable of measuring the spatial distribution of the energy-loss signal. We will therefore examine the situation for transmission-mode measurements, to see whether scattering delocalization offers the possibility of mapping a low-loss signal with reduced radiation damage.

2. Delocalization of inelastic scattering

TEM images and diffraction patterns arise from the *elastic* scattering of primary electrons by the electrostatic field of atomic nuclei. In a neutral atom, this field terminates on the surrounding atomic electrons and the scattering is localized to subatomic dimensions, allowing atomic-resolution images. The signal used in electron energy-loss spectroscopy (EELS) arises from the *inelastic* scattering by atomic electrons, which can be excited by a primary electron passing some distance away. This electron-electron scattering is therefore delocalized over a region of size $L(E)$, the delocalization length, whose value depends on the energy loss E involved in the scattering.

For valence-electron scattering ($1 \text{ eV} < E < 50 \text{ eV}$), $L(E)$ can be shown to be a few nm by recording the inelastic signal as a STEM probe is scanned across the edge of a specimen [4–8] or a sharp internal boundary [9]. Similar measurements for vibrational losses (0.1–0.5 eV) have given values of several tens of nm [1]. The general situation is illustrated in Fig. 1, which includes $L(E)$ values estimated from various kinds of TEM measurements (filled data points). The data is scattered (due to experimental error and the different methods, geometry and definitions used) but demonstrates how the delocalization distance is *inversely* related to energy loss.

For core-electron excitation, giving rise to an ionization edge at some hundreds of eV, $L(E)$ has subatomic dimensions but is important for the interpretation of channeling measurements on crystalline specimens [14–20]. This delocalization has been calculated using Bloch-wave or multislice methods [21–30] and is com-

E-mail address: regerton@ualberta.ca<http://dx.doi.org/10.1016/j.ultramic.2017.02.007>

0304-3991/© 2017 Elsevier B.V. All rights reserved.

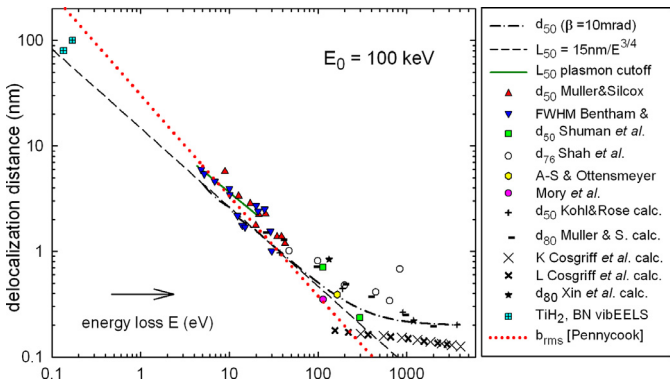


Fig. 1. Delocalization length $L(E)$, adjusted to an incident energy of $E_0 = 100$ keV, based on measurements [1–13] and calculations [24–30]. The dashed line represents Eq. (2) and the dotted red line is based on Eq. (4). (For interpretation of the references to color in this figure legend, the reader is referred to the web version of this article.)

plicated by the influence of elastic scattering, which occurs on a length scale similar to that of the core-loss scattering.

The lines in Fig. 1 are based on relatively simple considerations. For example, we can use the Heisenberg uncertainty principle $\Delta p_x \Delta x \approx h$ to estimate a delocalization distance Δx , taking the momentum uncertainty as $\Delta p_x = \pm(h/\lambda)\theta_{50}$, h being Planck’s constant, λ the primary-electron wavelength and θ_{50} the angular width containing 50% of the scattering. Assuming an inverse correlation between impact parameter and scattering angle, the length containing half of the inelastic scattering is:

$$\Delta x \approx h/(2\Delta p_x) \approx 0.5(\lambda/\theta_{50}) \quad (1)$$

Except for Cerenkov and surface-mode losses, inelastic scattering is dominated by a dipole component with a Lorentzian angular distribution of half-width $\theta_E \approx E/2E_0$ but with a cutoff around an angle θ_c , giving $\theta_{50} \approx (\theta_E \theta_c)^{1/2}$. A Bethe-ridge cutoff at $\theta_c \approx (2\theta_E)^{1/2}$ leads to:

$$\Delta x \approx 0.5\lambda/(\theta_E \theta_c)^{1/2} \approx (0.42)\lambda/(\theta_E)^{3/4} \approx (0.71)\lambda(E_0/E)^{3/4} \quad (2)$$

as indicated by the dashed line in Fig. 1. In this figure, the black dash-dot curve represents Eq. (2) combined (by quadrature addition) with the diffraction limit imposed by a 10 mrad spectrometer-collection aperture. The aperture effect is important only for large energy losses; for $E < 50$ eV, $\theta_E < 1$ mrad and almost all the inelastic signal passes through a typical aperture.

Invoking Fourier optics, we can compare the inelastic scattering of electrons with the diffraction of electrons of wavelength λ from a circular aperture of radius a . Observed on a distant screen, the first minimum in the Airy-function intensity corresponds to a deflection angle of $\theta_1 = 0.61\lambda/a$, which forms the basis of the Rayleigh criterion for resolution: $\Delta x = 0.61\lambda/\theta_1$. However, the angular range containing half of the photons is $\theta_{50} = 0.263(\lambda/a)$ and the diameter from which these photons emerge is $d_{50} = (2a)/2^{1/2}$, giving a value:

$$d_{50} \approx 0.37(\lambda/\theta_{50}) \approx (0.53)\lambda(E_0/E)^{3/4} \quad (3)$$

that is slightly smaller than Eq. (1).

Using $\Delta p_x \Delta x \approx h$ and similar arguments, Pennycook [17] obtained an expression for the root-mean-square (RMS) impact parameter b_{RMS} (weighted over the Lorentzian angular distribution) that can also be interpreted as a delocalization length:

$$b_{RMS} \approx (h/2\pi)(v/E)[\log_e(2/\theta_E)] \approx (h/2\pi)(v/E)[\log_e(4E_0/E)] \quad (4)$$

Eq. (4) predicts an energy-loss dependence close to E^{-1} rather than $E^{-3/4}$ but provides an equally good fit to experimental data, as shown in Fig. 1.

3. Point spread function for inelastic scattering

The success of Eq. (3) in predicting delocalization suggests using the methods of Fourier optics to relate the spatial distribution of the scattering (here denoted as a point-spread function, PSF) to its angular distribution, easily recorded as an intensity variation at a distant plane (Fraunhofer diffraction pattern). In light optics, the PSF is related to the Fourier transform of the angular distribution of scattered intensity or scattered amplitude, depending on the lateral coherence length of the illumination [31]. For the elastic scattering of electrons, the lateral coherence exceeds atomic dimensions and the object-plane potential is related to the scattered amplitude [32,33]. Extending this idea to the inelastic scattering of electrons suggests:

$$PSF(r) \propto [FT(dI/d\Omega)^{1/2}]^2 \quad (5)$$

where r is an object-plane radial coordinate and FT represents a two-dimensional Fourier transform. Under most conditions, the angular distribution of inelastic intensity is close to a Lorentzian function: $(dI/d\Omega) \propto (\theta^2 + \theta_E^2)^{-1}$, with an amplitude $(\theta^2 + \theta_E^2)^{-1/2}$ whose Fourier transform has a simple analytical form [34], giving:

$$PSF(r) \propto [FT(\theta^2 + \theta_E^2)^{-1/2}]^2 = (k_0 r)^{-2} \exp(-2\theta_E k_0 r) \quad (6)$$

where $k_0 = 2\pi/\lambda$ is the incident-electron wavenumber, making the product $k_0 r$ dimensionless. The exponential behavior at large r is consistent with aloof-EELS measurements of Muller and Silcox [7]. The $1/r^2$ dependence at small r agrees with calculations of inner-shell excitation by Ritchie [22] and Wentzel-potential estimates of Rose [21], summing over all energy loss.

Introducing a gradual cutoff of the Lorentzian angular distribution around some large angle (θ_c) makes Eq. (6) more realistic by removing the singularity at $r = 0$, and can be simulated by replacing the $1/r^2$ dependence in Eq. (6) by a Lorentzian function, so that:

$$PSF(r) \propto (r^2 + r_c^2)^{-1} \exp(-2\theta_E k_0 r) \quad (7)$$

where $r_c = (2k_0\theta_c)^{-1}$. Fig. 2 indicates that Eq. (7) is a reasonable match to the PSF calculated using Eq. (5).

4. Properties of the inelastic PSF

The inelastic point spread function can be specified more precisely in terms of the probability ($d^2P/dEdV$) that a primary electron interacts with a volume dV of specimen, located at a radial distance r from the path of the primary electron and resulting in an energy loss between E and $E + dE$. Based on Eq. (7):

$$d^2P/dEdV = C(r^2 + b_{min}^2)^{-1} \exp(-2r/b_{max}) \quad (8)$$

where C is an E -dependent coefficient (to be determined) and

$$b_{max} = 1/(k_0\theta_E) = 1/[(2\pi mv/h)(h\omega/2\pi)/(mv^2)] = v/\omega \quad (9)$$

The quantity b_{max} is known as the Bohr adiabatic limit because at larger distances ($r \gg b_{max}$) the electrostatic field induced by the primary electron changes slowly enough to allow atomic electrons to respond adiabatically, without absorbing energy. In fact, the inelastic interaction starts to fall off exponentially at $r \approx b_{max}/2$, as indicated by Eq. (8). This behavior has been called dynamical screening [7] and is directly related to the characteristic angle of the inelastic scattering: $\theta_E = E/(mv^2)$, as seen from Eq. (9).

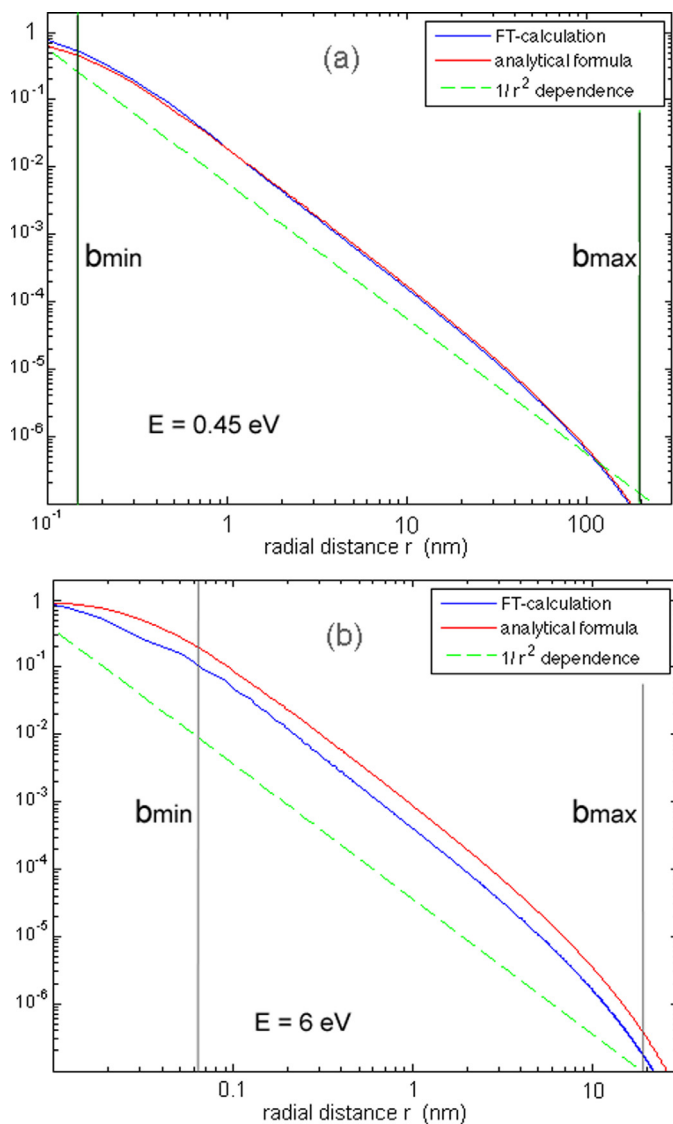


Fig. 2. Point-spread function for inelastic scattering with (a) $E = 0.45$ eV and $E_0 = 60$ keV, (b) $E = 6$ eV and $E_0 = 200$ keV. The blue curves were calculated using Eq. (5), assuming $dI/d\Omega \propto (\theta^2 + \theta_E^2)$, with gradual (Lorentzian) cutoff around $\theta_c = (2\theta_E)^{1/2}$. Red curves are calculated from Eq. (7) and green dashed lines depict $1/r^2$ behavior. Vertical lines show the values of b_{\min} and b_{\max} . (For interpretation of the references to color in this figure legend, the reader is referred to the web version of this article.)

The length b_{\min} arises because the angular distribution of dipole-mode scattering remains Lorentzian only up to some angle θ_c such that:

$$b_{\min} \approx 1/(2k_0\theta_c) = (b_{\max}/2)(\theta_E/\theta_c) \quad (10)$$

In the case of plasmon excitation, θ_c is the angle at which momentum conservation allows the transfer of energy to single-electron transitions at the Fermi energy, leading to heavy plasmon damping. In the case of single-electron excitation, $\theta_c \approx (E/E_0)^{1/2} \approx (2\theta_E)^{1/2}$ is the Bethe-ridge angle at which momentum conservation permits energy transfer to a free electron, rather than inducing dipole transitions. In the case of vibrational-EELS peaks (in the range 0.1 eV–0.5 eV), θ_c may be the angle at which dipole transitions give way to impact scattering. Because this angle is currently unknown, we will use a Bethe-ridge cutoff since it gives approximate agreement with measured delocalization lengths, represented by the square data points on the left in Fig. 1.

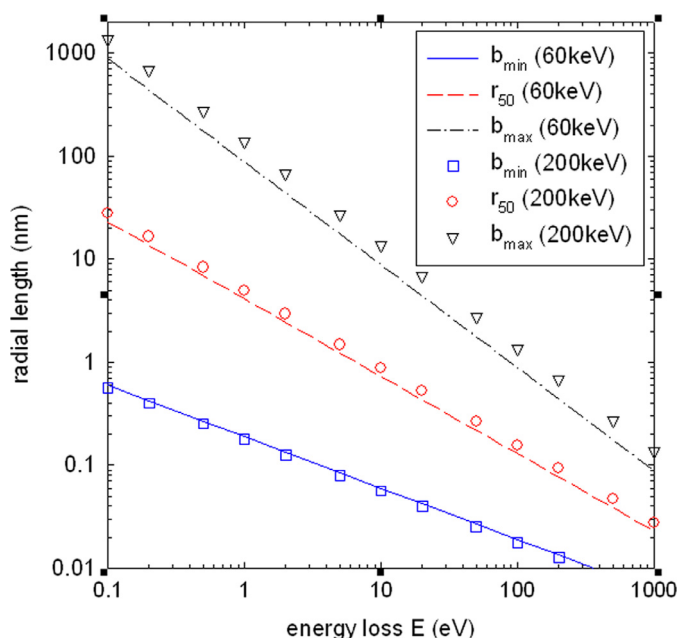


Fig. 3. Values of b_{\min} , b_{\max} and r_{50} calculated from Eqs. (9)–(13) as a function of energy loss E , for $E_0 = 60$ keV and 200 keV. An angular cutoff at $\theta_c = (E/E_0)^{1/2}$ is assumed, giving $b_{\min} \propto E^{-1/2}$, $b_{\max} \propto 1/E$ and r_{50} proportional to $E^{-3/4}$ but nearly independent of E_0 .

As seen in Fig. 3, the ratio b_{\max}/b_{\min} is typically in the range 10–50 for inner-shell excitations (core losses), of the order of 100 for plasmon and valence-electron excitation and as high as 500 for vibrational losses [3]. So for low energy losses, the inelastic PSF is close to a $1/r^2$ power law over much of its range, with (typically) less than 10% of the intensity lying below $r = b_{\min}$ and less than 5% above $r = b_{\max}/2$. Therefore the probability that inelastic scattering occurs inside a radius r is roughly

$$(dP/dE)_{<r} \approx \int (C/r^2)dV = C \log_e(r/b_{\min}) \quad (11)$$

and the probability that it lies outside this radius r is approximately

$$(dP/dE)_{>r} \approx \int (C/r^2)dV = C \log_e(b_{\max}/2r) \quad (12)$$

where we have integrated Eq. (8), taking $dV = (2\pi r t)dr$ with t representing specimen thickness. Equating these two integrals provides an estimate for the median radius r_{50} , containing 50% of the inelastic scattering with energy loss E :

$$r_{50} \approx (b_{\min} b_{\max}/2)^{1/2} \quad (13)$$

For valence or core-electron excitation, where $\theta_c \approx (E/E_0)^{1/2} \approx (2\theta_E)^{1/2}$, the diameter containing half the scattering is therefore:

$$d_{50} = 2r_{50} = 2k_0^{-1}(4\theta_E\theta_c)^{-1/2} = 0.16\lambda/(\theta_E\theta_c)^{1/2} \quad (14)$$

This result is similar in form to Eq. (3) but about a factor of 2 smaller, suggesting that Eq. (5) might underestimate the spatial extent of delocalization. However, we will continue with the coherent approximation for now and return to the question of accuracy later.

Integrating Eq. (8) from $r = b_{\min}$ to $r = b_{\max}/2$, equivalent to replacing the exponential attenuation with a sharp cutoff at $b_{\max}/2$, gives:

$$\begin{aligned} dP/dE &= C \int (r^2 + b_{\min}^2)^{-1} (2\pi r t) dr \\ &= (\pi C t) \int (r^2 + b_{\min}^2)^{-1} d(r^2 + b_{\min}^2) \end{aligned}$$

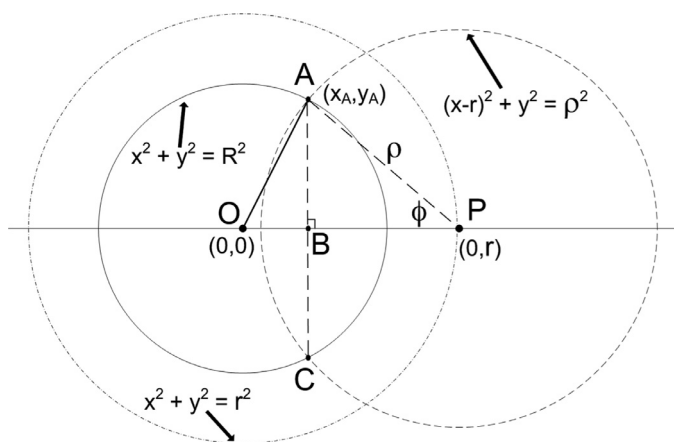


Fig. 4. Incident electron probe (solid circle, radius R) and geometry needed to calculate the inelastic intensity at point P , a distance r from the center of the probe.

$$\begin{aligned} &\approx (\pi Ct) \log_e \left[(b_{\max}^2/4 + b_{\min}^2)/b_{\min}^2 \right] \\ &= (\pi Ct) \log_e (1 + \theta_c^2/\theta_E^2) \end{aligned} \quad (15)$$

where t is specimen thickness and Eq. (10) has been used for b_{\max}/b_{\min} . Eq. (15) is of identical form to the result obtained from the dielectric theory of energy loss:

$$dP/dE = t(\pi a_0 m_0 v^2)^{-1} \text{Im}[-1/\varepsilon(E)] \log_e (1 + \theta_c^2/\theta_E^2) \quad (16)$$

where $a_0 = 52.9$ pm is the Bohr radius, m_0 is the electron rest mass and v is the speed of the primary electrons [35]. $\text{Im}[-1/\varepsilon(E)]$ is the energy-loss function, which can be calculated if the permittivity ε of the specimen is known at a photon frequency E/h , but which becomes a constant factor if we want to describe the spatial dependence of dP/dE at a fixed value of energy loss.

Eq. (15) was derived by integration over real space, whereas Eq. (16) comes from integration of reciprocal space. Equating these two expressions gives the coefficient used in Eq. (8) as $C = (\pi^2 a_0 m_0 v^2)^{-1} \text{Im}[-1/\varepsilon(E)]$, allowing the inelastic PSF to be written as:

$$\begin{aligned} d^2P/dEdV &= (\pi^2 a_0 m_0 v^2)^{-1} \text{Im}[-1/\varepsilon(E)] (r^2 + b_{\min}^2)^{-1} \\ &\times \exp(-2r/b_{\max}) \end{aligned} \quad (17)$$

5. Electron beam of arbitrary radius

In the case of a broad incident beam, each primary electron has its own PSF that describes the spatial extent of energy loss. In the center of the beam these functions overlap to create a uniform rate of scattering and energy deposition. At the edge of the beam, the PSF tails extend into the surrounding material, to an extent that depends on the energy loss E . The fraction of scattering outside the incident probe will be largest in the case of a small-diameter probe and a low value of E .

We will assume that the spatial distribution of inelastic scattering is a two-dimensional convolution of the inelastic PSF with the current-density profile of the beam. For convenience, we take the latter to be a rectangular (top-hat) function.

The geometry involved in the convolution is shown in Fig. 4. The incident beam has a radius R and is centered on the origin of the coordinate system. We first calculate the intensity I_p of inelastic scattering at a point P outside the probe, allowing for electrons incident at all points within the area A_p of the probe. This can be done by summing over the incident intensity within arcs AC (of radius ρ and thickness $d\rho$), using the fact that point A lies the intersection of circles of radius ρ and R and therefore has a coordinates:

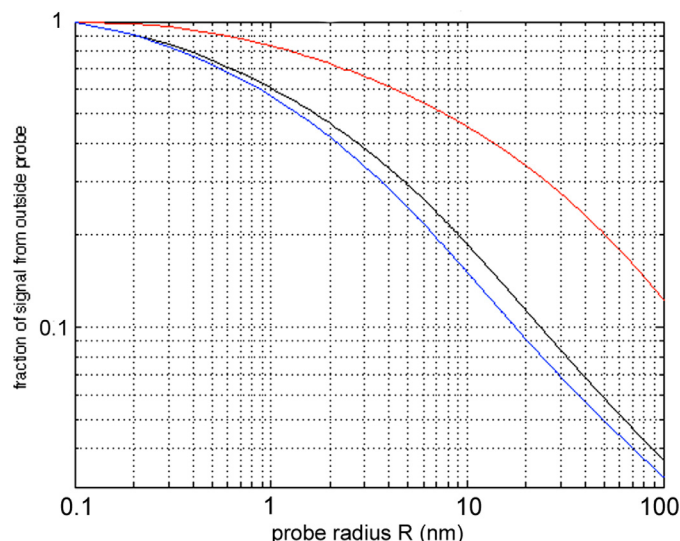


Fig. 5. Fraction of the inelastic scattering occurring outside an electron probe of radius R . Upper red curve: $E = 0.45$ eV, $E_0 = 60$ keV; middle black curve: $E = 6$ eV, $E_0 = 200$ keV; lower blue curve: $E = 6$ eV, $E_0 = 60$ keV. (For interpretation of the references to color in this figure legend, the reader is referred to the web version of this article.)

$x_A = (R^2 + r^2 - \rho^2)/(2r)$ and $y_A = (R^2 - x_A^2)^{1/2}$. From geometry of the triangle ABP , $\sin(\phi) = (y_A/\rho)$ and the length of arc AC is $S = 2\phi\rho$. The number of incident electrons per second contained within the arc-shaped region is $J_e S(d\rho)$, where $J_e = I_e/(\pi R^2)$ for a beam current I_e electrons/s and a uniform current density J_e electrons/m²/s. The number of electrons/m²/s inelastically scattered at point P is therefore:

$$I_p(r) = J_e t \int (d^2P/dEdV) dA_p = J_e t \int S(d^2P/dEdV) d\rho \quad (18)$$

where the limits of integration are from $\rho = r - R$ to $\rho = r + R$. The total signal (electrons/s) from inelastic scattering outside the probe is given by a second integration:

$$I_{\text{sig}}(R) = \int I_{(r)}(2\pi r) dr = \int I_p(r)(2\pi r^2) d[\log_e(r)] \quad (19)$$

where the integration is from $r=R$ to $r > R + b_{\max}$. The use of a logarithmic grid to evaluate Eq. (25) helps in achieving accuracy (within a short computing time) for a large range of signal radius r .

Fig. 5 shows the fraction of the inelastic signal originating from outside the probe, calculated using Eq. (19). For 60 keV electrons, this fraction remains appreciable ($> 10\%$) for probe radii up to about 17 nm ($E = 6$ eV) or 150 nm (at $E = 0.45$ eV). If Eq. (8) is accurate for small r , about 84% of the 0.45 eV scattering and 57% of the 6 eV scattering lies outside a 60 keV probe of radius 1 nm (diameter = 2 nm). Fig. 5 also demonstrates how the delocalization depends strongly on the energy loss E but only weakly on the incident energy E_0 [35].

The preceding equations assume a parallel incident beam, whereas the very small probes involved in STEM can have an appreciable convergence semi-angle α . From the point of view of the spatial distribution of scattering, the main effect of this convergence is probably an increase in beam diameter, by an amount αt at the top and bottom surfaces if the probe is focused at the midplane of a specimen of thickness t , giving an increase $\alpha t/2$ if averaged over the thickness of the film. For small probes this effect could be significant and might be incorporated approximately by adding $\alpha t/2$ to the value of R used in Eqs.(18) and (19).

For an incident beam of large radius, the rate of inelastic scattering will be uniform in the center but decreases towards the

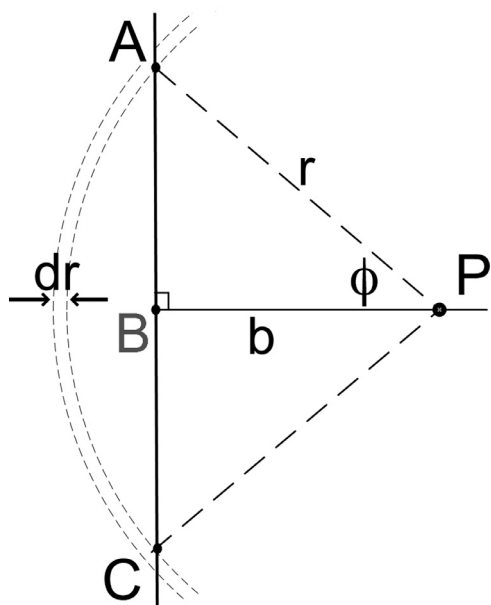


Fig. 6. Geometry for calculating the inelastic intensity at point P, a distance b outside the edge ABC of an electron beam of large radius. The contributions of arcs of specimen AC (radius r , thickness dr) are summed over r to give the total EELS signal at point P.

edge and beyond it. For $R \gg L(E)$, the edge approximates to a straight edge and the geometry simplifies to that shown in Fig. 6. The intensity beyond the edge of the beam is still given by integration over arcs AC whose length is $S = (2\varphi r)$, with $\varphi = \arccos(b/r)$. The inelastic intensity (electrons/m²/s) at a distance b outside the edge is then:

$$I(b) = J_e t \int (d^2P/dE dV) (2\varphi r) dr \quad (20)$$

where J_e is the current density (electrons/m²/s) within the probe and the integration limits are from $r=b$ up to some large value ($> b_{\max}$). Within the illuminated area, the intensity at a distance b inside the edge is $I(-b) = I(0) - I(b)$, giving a symmetric intensity profile, as shown in Fig. 7.

It is tempting to apply Eq. (17) to the case of a small-diameter aloeof beam at point P, a distance b from the edge AC of the specimen, integrating from $r=b$ to some large value in order to calculate the energy-loss signal $S(b)$ as a function of the impact parameter b . This would allow comparison with measurements of $S(b)$ for vibrational EELS [1] and valence-electron excitation [7,8]. But the electric field of an aloeof electron lacks the radial symmetry of the PSF and this situation involves surface modes, which may make such a comparison inaccurate. In any event, the form of $S(b)$ appears to be well matched [1] by the formula:

$$S(b) \propto (m_0 v^2)^{-1} K_0(4\pi b E / [\gamma v h]) = (m_0 v^2)^{-1} K_0(2\theta_E k_0 b) \quad (21)$$

derived from the dielectric response to an electron traveling parallel to a planar surface [36–38].

6. Point spread function for energy deposition

Radiation damage to a beam-sensitive TEM specimen arises predominantly from inelastic scattering, through the process referred to as radiolysis [33,39,40]. This same process is responsible for the damage caused by x-rays, and in both cases the amount of damage is believed to be proportional to the energy deposited per unit volume of specimen. Almost all inelastic events contribute to this energy deposition, but in proportion to the energy loss suffered in each event, so the energy H deposited per unit volume V

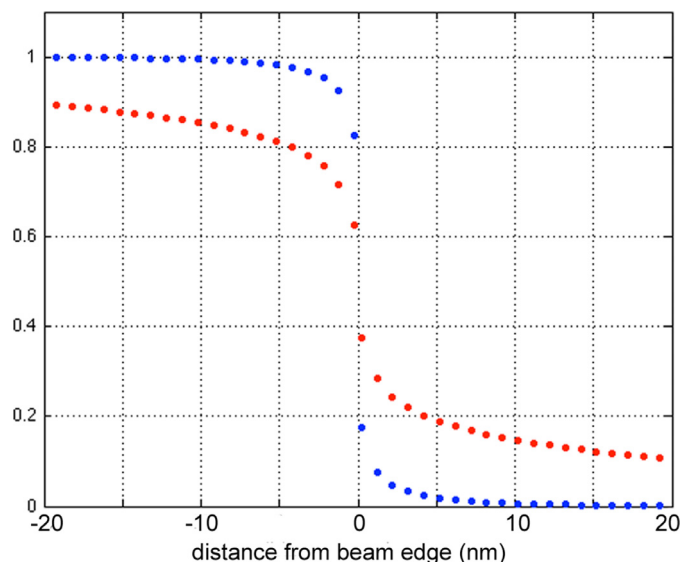


Fig. 7. Inelastic intensity near the edge of an electron beam of large radius and uniform intensity. Blue data points correspond to $E = 6$ eV, red data points to $E = 0.2$ eV. The calculations assume an incident energy of $E_0 = 100$ keV. (For interpretation of the references to color in this figure legend, the reader is referred to the web version of this article.)

by a single primary electron is:

$$dH/dV = \int E (d^2P/dE dV) dE \quad (22)$$

where P represents the probability of an energy loss E per primary electron, as in Eq. (8), and the integral is from some threshold energy loss ($E_{\min} \sim 5$ eV) to a large value, which can be taken as 100 eV [3]. In the case of a STEM probe, both P and H are functions of the distance r , measured from the center of the probe.

In Eq. (22), dH/dV has units of eV/m³ but multiplying by $e = 1.6 \times 10^{-19}$ converts dH/dV into J/m³. Dividing by the specimen density ρ (in kg/m³) then gives the local radiation dose $g(r)$ per primary electron, expressed in Gray:

$$g(r) = e(dH/dV)/\rho \quad (23)$$

To relate $g(r)$ to the case of an electron probe whose diameter is much less than the delocalization length, we can multiply $g(r)$ by the number of primary electrons to get the radiation dose $G(r)$ at a distance r from the beam:

$$G(r) = e(dH/dV)\rho^{-1}(I_b/e)T = (dH/dV)\rho^{-1}I_b T \quad (24)$$

where I_b is the primary-beam current in Amp, (I_b/e) is the current in electrons/sec, and T is the irradiation time in sec.

With $(d^2P/dE dV)$ given by Eq. (17), both dH/dV and the dose $G(r)$ will decrease with increasing radius r from the beam. High- E scattering causes energy deposition at small r and low- E scattering at larger distances from the probe, but the local extent of radiolysis depends only on the total energy deposition per kg, as described by Eqs. (24), (22) and (17). Radiation damage starts within the probe and gradually spreads outwards.

To calculate $G(r)$ we should sum over a range of energy loss, using Eqs. (22) and (17), which requires a knowledge of the energy-loss function $\text{Im}[-1/\epsilon(E)]$. The latter can be obtained from the energy-loss spectrum $S(E)$ of the specimen, measured with a broad electron beam and a collection aperture of semiangle β , based on the standard dielectric theory [35]:

$$S(E) = I_b t (\pi a_0 m_0 v^2)^{-1} \text{Im}[-1/\epsilon(E)] \log_e(1 + \beta^2/\theta_E^2) \quad (25)$$

where (as elsewhere in this analysis) we assume that the specimen thickness t is small enough to make plural inelastic scattering unimportant.

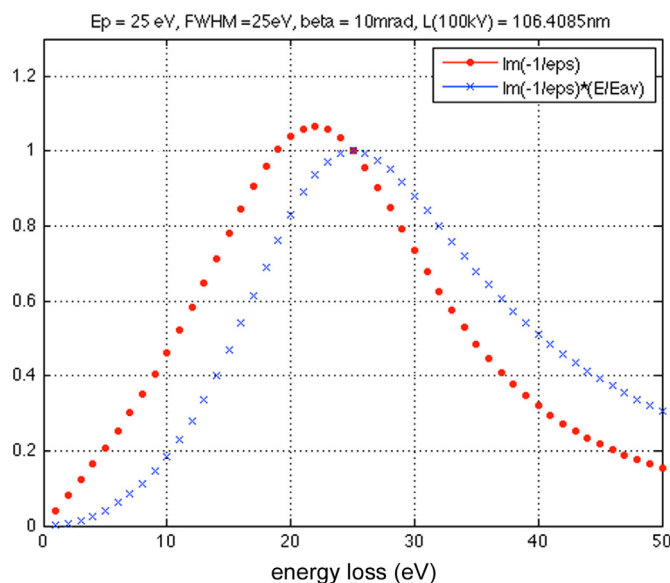


Fig. 8. Red dots: energy-loss function $\text{Im}[-1/\varepsilon(E)]$ for a typical organic specimen (calculated using a Drude model), representing the variation of scattering probability with energy loss. The corresponding inelastic mean free path is $\lambda_i = 170$ nm at $E_0 = 200$ keV. Blue crosses show the product $(E/E_{av}) \text{Im}[-1/\varepsilon(E)]$, where $E_{av} = 26$ eV, which represents the corresponding energy deposition in a thin specimen (single-scattering approximation).

Alternatively, the energy-loss function can be simulated by using the Drude model for valence-electron excitation:

$$\text{Im}[-1/\varepsilon(E)] = [E(\Delta E_p)E_p^2] / [(E^2 - E_p^2)^2 + (E\Delta E_p)^2] \quad (26)$$

where E_p and ΔE_p are the energy and width of the valence-loss peak [35]. In using Eq. (26), we neglect the energy deposition arising from inner-shell excitation, which is of lesser importance in light-element solids.

Taking $E_p = 25$ eV and $\Delta E_p = 25$ eV gives an energy-loss function (Fig. 8) that is typical of an organic compound and this function was used in the present calculations. The mean energy loss is 26 eV, defined by:

$$E_{av} = \int E \text{Im}[-1/\varepsilon(E)] dE / \int \text{Im}[-1/\varepsilon(E)] dE \quad (27)$$

K-shell excitation increases E_{av} to typically 35–40 eV in an organic compound, but inner-shell energy deposition occurs very close to the electron probe and in practice be indistinguishable from energy deposition within the probe. More generally, $E_{av} \approx 7Z$ and becomes large in materials of high atomic number Z , due to inner-shell contributions [35]. However, most of these materials are less radiation-sensitive.

Calculated using Eqs. (17), (22) and (26), Fig. 9 shows the fraction of energy deposited (within an organic specimen) outside an electron beam of a given diameter. This fraction increases slightly with primary-beam energy because of the increasing delocalization length.

When energy deposition occurs within a beam-sensitive specimen, radiolysis causes a characteristic signal (e.g. diffracted intensity or an energy-loss peak) to diminish with increasing radiation dose G , usually in an exponential manner. We therefore assume that the radial distribution of the EELS signal (energy loss E) after an exposure time T is described by:

$$\text{PSF}(r, E, T) = \text{PSF}(r, E, 0) \exp[-G(r)/G_c] \quad (28)$$

where $G(r)$ is the radiation dose at a distance r from the probe; G_c is a characteristic (or critical) dose, measured using a broad electron beam, which is an inverse measure of the radiation sensitivity

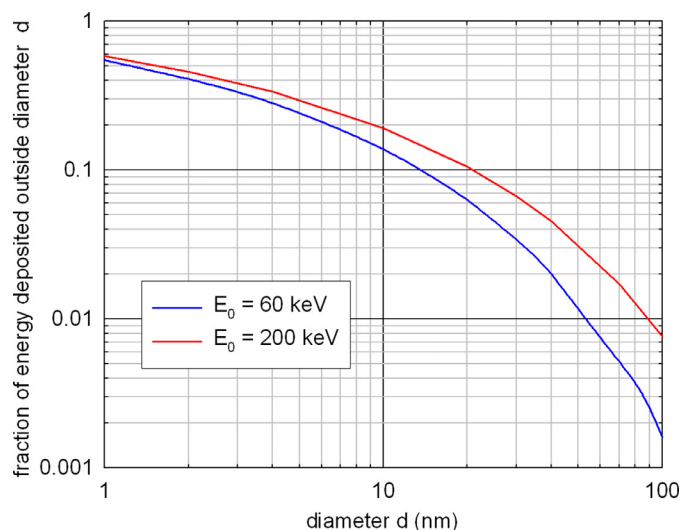


Fig. 9. Fraction of energy deposited outside an electron beam of diameter d , calculated on the basis of Eqs. (17) and (19), assuming a uniform current density within the beam and the energy-loss function shown in Fig. 10.

of the specimen. In Eq. (28) we assume that radiation damage does not significantly change the inelastic scattering within the specimen.

Electron microscopists commonly measure radiation dose as an electron fluence, the product of beam-current density and exposure time: $D = JT$ where D is in C/m^2 , or $D_e = J_e T$ where D_e is in electrons/ m^2 . The corresponding dose in Gray is:

$$G = (D_e/\rho) e(dE/dz) = (D/\rho)(E_{av}/\lambda_i) \quad (29)$$

where dE/dz is the linear energy transfer (LET) or stopping power (in eV/m), which can be calculated by dividing the mean energy loss E_{av} per inelastic collision (in eV) by the mean distance λ_i between collisions.

Expressed in Gray, the characteristic dose G_c varies greatly between different materials but is independent of electron energy E_0 . Because λ_i increases with increasing E_0 , the corresponding characteristic fluence D_c depends on both the material and the electron energy. Typical values for a beam-sensitive polymer are $G_c = 25$ MGy and $E_{av} = 35$ eV, giving $dE/dz = 2.5 \times 10^8$ eV/m and $D_c = 100$ C/m^2 at $E_0 = 100$ kV.

Fig. 10 shows the effect of radiolysis due to a small-diameter (sub-nm) beam of electrons traveling through an organic specimen, calculated using Eqs. (28), (17) and (26). Blue curves represent the radial dependence of energy deposition, which is more localized than either the 6 eV or 0.45 eV signals since the average energy loss exceeds 25 eV. Green curves, based on Eq. (17), demonstrate the increased delocalization at lower energy loss, as in Figs. 1 and 2. The red curves show how radiolysis reduces the energy-loss signal generated close to the center of the electron probe, the signal from larger distances being hardly affected. This behavior is particularly evident for vibrational-mode losses ($E < 0.5$ eV, Fig. 10a), where the delocalization distance $L(E)$ is tens of nm.

7. Damage measurements on polymers

The energy-loss spectra of organic materials contain a broad peak centered around 20–25 eV (as in Fig. 8), usually interpreted as a highly-damped plasmon resonance of the valence electrons. Compounds with double bonds also exhibit a smaller peak at 6–7 eV, attributed to π - π^* interband transitions. The presence of this peak indicates π -bonding and its fading during electron irradiation provides evidence of bond scission due to radiolysis. Among many

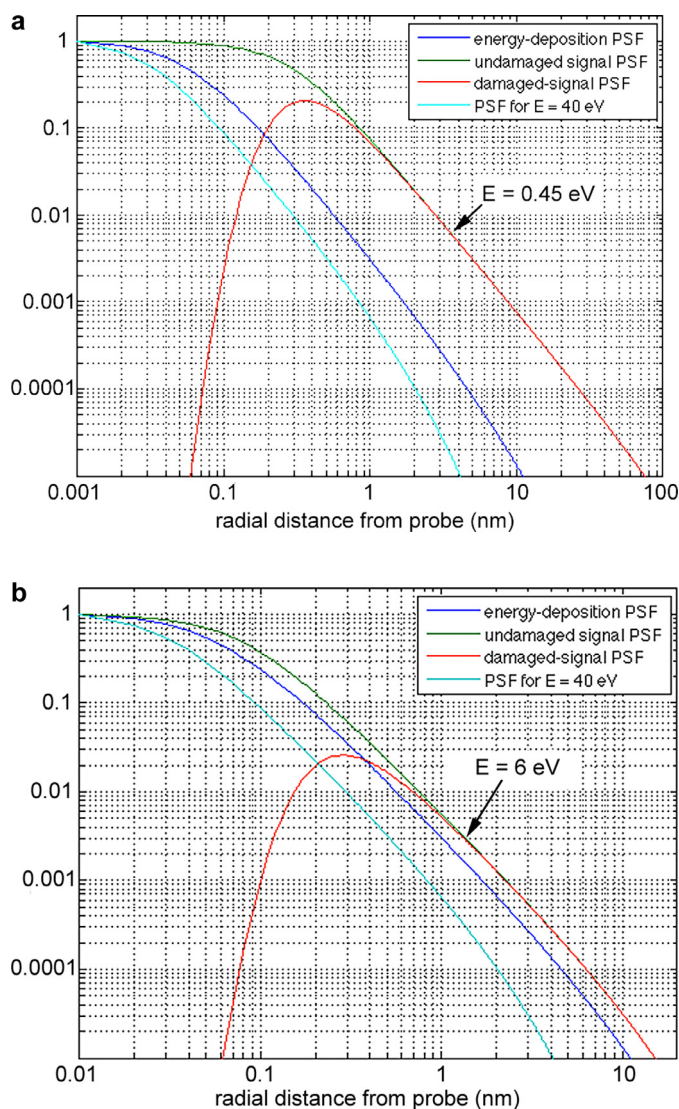


Fig. 10. Dark blue curves: PSF for energy deposition, calculated using Eq. (27) for a beam-sensitive specimen having the energy-loss function shown in Fig. 4. For comparison, light blue curves show the PSF for $E = 40$ eV, the mean energy loss for a typical organic compound. Green curves are the PSF from Eq. (17), for an energy-loss signal at (a) 0.45 eV and (b) 6 eV, assuming no damage. Red curves are based on Eq. (22) and Eq. (28), and show the spatial distribution of the EELS signal after substantial damage has occurred around the electron probe. (For interpretation of the references to color in this figure legend, the reader is referred to the web version of this article.)

radiation-damage investigations of polymers are studies [41–43] in which the intensity I_{π^*} of the π^* peak was monitored as a function of irradiation time, for a fixed beam current I_b but using different values of the electron-beam diameter d . Plotting $\log(I_{\pi^*})$ against irradiation time yielded a characteristic time T_c (for double-bond scission) that initially decreased as d was reduced (as expected from the increased current density) but remained nearly constant for $d < 100$ nm. If a characteristic dose (fluence) is calculated as $D_c = (\pi/4)(I_b/d^2)T_c$, constancy of T_c implies D_c increasing proportional to $1/d^2$, by a factor as large as 10^6 at $d = 0.3$ nm [43]. Further experiments, in which I_b was varied at constant d , showed that this unexpected behavior was not a dose-rate effect (D_c dependent on J) but was directly related to beam diameter.

This apparent reduction in radiation sensitivity (for small probes) assumes that all of the energy deposition occurs within the incident beam, which ignores the delocalization of inelastic scattering. Because of the huge current density, the initial damage

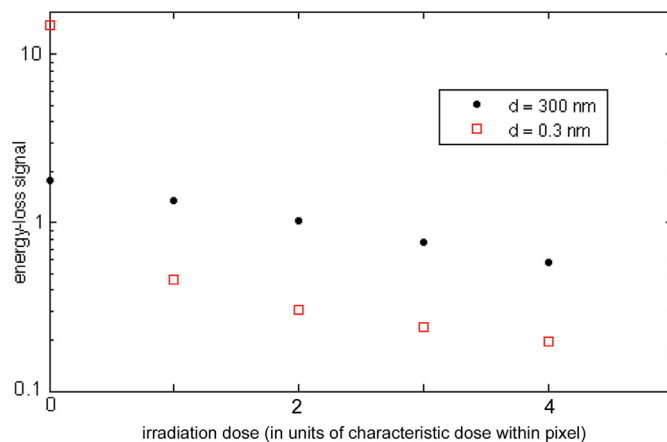


Fig. 11. Time dependence of the 6 eV π^* energy-loss peak recorded from polystyrene, for 300 keV incident electrons and beam diameters of 300 nm and 0.3 nm. The calculations take account of damage and signal generated outside the probe (due to the delocalization of inelastic scattering) but not damage arising from secondary electrons. (For interpretation of the references to color in this figure, the reader is referred to the web version of this article.)

within a small probe is very rapid, so what was measured (over a period of a few seconds) must correspond to the slow decay of the 6 eV signal from regions of specimen *outside* the probe.

Fig. 11 shows the result of PSF calculations designed to model the experiments on polystyrene [43], where the beam current was adjusted to give a 2.5-fold decay in the π^* intensity (over 5 s) for $d = 300$ nm, represented by the black circular data points. The case of a very small (0.3 nm) probe is represented by the red-square data points, the first of which would be unobservable since it corresponds to zero dose (undamaged specimen). Subsequent red data points show a slope very similar to that for $d = 300$ nm, leading to a time constant T_c independent of beam diameter, just as observed experimentally.

The fact that T_c remained constant for beam diameters as large as 100 nm is at first surprising. The diameter $2b_{\max}$ within which the 6 eV signal is generated is about 64 nm at $E_0 = 300$ keV but would be larger if Eq. (5) underestimates the delocalization. In fact, a large part (e.g. 80%) of the radiolysis of organic materials is known to arise from secondary-electron production [44]. A simplified analysis [45] of fast-secondary ($E > 50$ eV) transport suggests a mean range of the order of 10 nm, consistent with Monte Carlo calculations [42] and PMMA lithography [46]. So secondary electron production increases the damage outside a small probe but probably not very much, compared to the delocalization of inelastic scattering.

8. Optimization of the signal/damage ratio

The possibility of exploiting delocalization to obtain an energy-loss signal with less damage has been discussed for the case of aloof-beam spectroscopy [47,48], particularly in relation to the damage caused by inner-shell excitations. Reduced damage was subsequently demonstrated for aloof-beam EELS using a vibrational-mode signal [2], where calculations suggest that the signal/damage ratio may increase by a factor of 10^5 as the impact parameter b (distance of the beam from the specimen edge) is increased from 10 nm to 60 nm [3]. The penalty associated with increasing b is a loss of spatial resolution, since the specimen area contributing to the energy-loss signal is of the order of $(2.5)b^2$ [3].

A tradeoff between damage and resolution is familiar in electron microscopy: for a broad beam (diameter d) of electrons traveling *through* a specimen, the radiation dose is proportional to $1/d^2$, for a given beam current and recording time. So a six-fold increase in diameter should improve the signal/damage ratio by a factor of

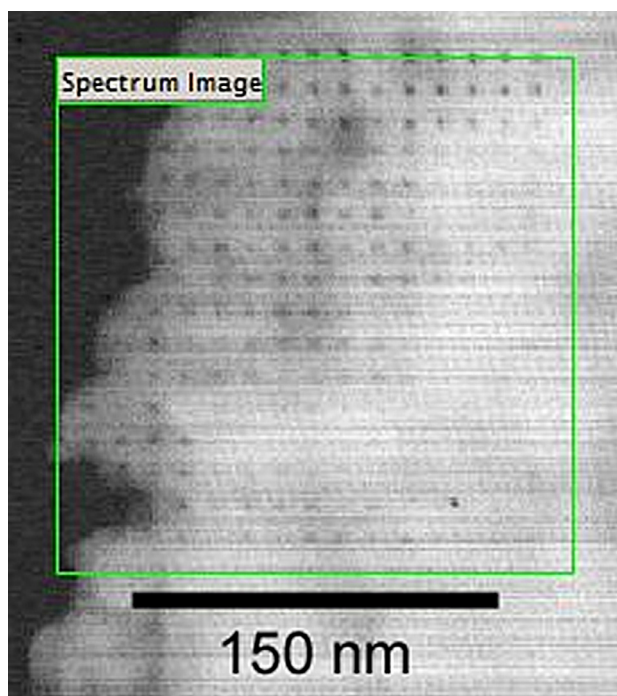


Fig. 12. Finely-scanned HAADF image showing the effect of using a coarse digital raster ($s = 10$ nm, $d = 1$ nm) on a specimen of $\text{Ca}(\text{OH})_2$. Dark spots show locations where the electron beam caused mass loss due to radiation damage, while the hydrogen vibEELS signal remained largely unaltered after three complete scans. (For interpretation of the references to color in this figure, the reader is referred to the web version of this article.)

36 in transmission mode. The much larger improvement in a loof mode arises because the total energy deposition is much less; energy that would be deposited in the specimen within a few nm of the electron probe is no longer deposited if the primary electrons are traveling in a vacuum.

The a loof mode is attractive for spectroscopy of beam-sensitive specimens but it lacks the ability to map the two-dimensional distribution of the signal. Transmission-mode STEM measurements can perform such mapping but only if radiation damage does not destroy the signal, a major limitation if the specimen is beam-sensitive.

The usual way of creating a STEM image is to scan a small probe (diameter d) in the form of a digital raster with a jump distance s (pixel spacing) approximately equal to d . The case of $s > d$ represents undersampling and is usually avoided because the irradiated area is then only a fraction of the scanned area, suggesting increased radiation damage. For lower-magnification images, sub-pixel scanning is sometimes used to address this problem and reduce the damage. While this strategy may well be advantageous for core-loss images or x-ray elemental maps, low-loss images represent a different situation because of the greater delocalization of the signal. Undersampling might then be favorable because the regions between the directly-irradiated areas can contribute to the energy-loss signal, while suffering relatively little damage [49].

To illustrate this possibility, Fig. 12a shows a quickly-scanned HAADF image of a calcium hydroxide specimen, recorded using the Nion HERMES STEM at Arizona State University. This instrument incorporates a high-resolution monochromator and energy-loss spectrometer, giving an energy resolution (< 15 meV at $E_0 = 60$ keV) sufficient to detect vibrational-mode energy-loss peaks that are characteristic of hydrogen or specific chemical bonds [1]. The region within the green square was previously scanned using a coarse digital raster ($s = 10$ nm, $d = 1$ nm) and with a probe current high enough to cause substantial radiation damage, visible as

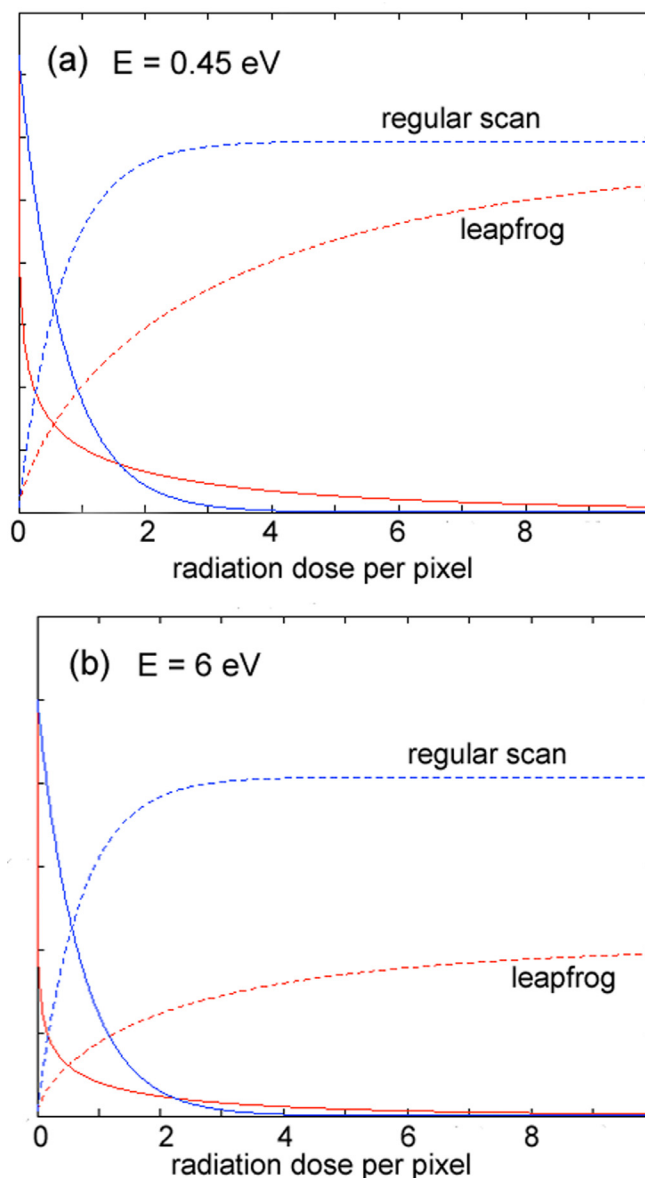


Fig. 13. Energy-loss signal as a function of dose D per pixel (in units of the characteristic dose) for a regular scan ($d = s = 30$ nm, blue curves) and leapfrog scan ($d \ll s = 30$ nm, red curves). Solid lines show the signal per pixel, dashed lines give the time-integrated signal. The incident energy is (a) 60 keV and (b) 300 keV. (For interpretation of the references to color in this figure legend, the reader is referred to the web version of this article.)

dark spots that indicate reduced specimen thickness (mass loss). Despite this localized damage, the 0.45 eV vibrational peak (due to hydrogen) remained almost constant.

Subsequent “leapfrog” scanning of guanine [50] showed a similar array of dark spots (indicating substantial damage within the 1 nm probe) and little decrease in the H-bond (0.3–0.4 eV) signal, but only if the step size was increased from $s = 10$ nm to $s = 30$ nm. However, increasing s reduces the spatial resolution of the image; for leapfrog scanning to be beneficial, it must provide a larger signal for the same spatial resolution.

Fig. 13a shows the predicted decay of the H-bond signal (integrated over a diameter s) as a function of irradiation dose D per pixel, based on the theory presented above. For a regular scan ($d = s$) the energy-loss signal falls exponentially with increasing radiation dose. For a leapfrog scan ($d \ll s$), it falls more rapidly but then more slowly as signal is collected (via scattering delocalization) from largely undamaged material between each beam posi-

tion. For $D > 2$, the leapfrog signal exceeds that from the regular scan and this advantage becomes more dramatic as the irradiation continues. However, the time-integrated signal from the leapfrog scan remains less than that from the regular scan, so the leapfrog image will be more noisy, degrading the *effective* spatial resolution (approximately s for both types of scan).

The situation for a 6 eV signal (e.g. π^* peak, characteristic of double bonds) is illustrated in Fig. 13b. Once again, the leapfrog signal is higher for a large dose but the corresponding time-integrated signal is only about half that for a regular scan.

9. Discussion

We have confined our attention to energy losses due to valence-electron or phonon excitation, where the delocalization distance is much larger than atomic dimensions and is determined by b_{\max} and the $1/r^2$ dependence of the point spread function. These properties derive from the kinematics of electron interaction rather than internal dynamics of an atom, as expressed in terms of the generalized oscillator strength for example [51]. Such dynamical effects will influence the PSF for $r < b_{\min}$ but this contribution to the inelastic signal is small for low values of energy loss.

The situation is different for inner-shell losses, where the region $0 < r < b_{\min}$ represents a larger part of the PSF and greatly affects the probability of core-electron excitation. Here the delocalization lengths of inelastic and elastic scattering are comparable to each other, producing a coupling that complicates the interpretation of atomic-resolution inelastic images recorded from crystalline specimens. Such complications are unlikely to be important for the low energy losses considered here.

Vibrational (phonon) energy losses have been studied for many years using medium-energy electrons reflected from the surfaces of crystalline specimens [52]. The EELS signal is found to contain two components: a dipole mode concentrated around Bragg-reflected beams, and an “impact” component that can be measured between the Bragg beams [53,54]. The latter has a broad angular distribution, indicating a high degree of localization around atomic cores. In fact, calculations of the transmission-mode phonon signal have predicted atomic resolution [55–58] and recent STEM measurements have confirmed that a resolution better than 2 nm is possible [59]. These measurements were made (using a crystalline BN specimen) in a dark-field mode, with the incident beam tilted so that the central and diffracted beams were intercepted by the spectrometer entrance aperture, giving a high-resolution signal about 1% of the bright-field phonon signal. Under such conditions, the equations derived above will not apply; we have assumed bright-field spectroscopy in which the dipole signal is predominant.

The theory presented here derives from Eq. (5), which assumes a coherent summation of amplitudes, ignoring any change of phase with scattering angle. This assumption may be correct for excitations to a bound state [12] but is questionable for excitation to a continuum, which involves a degree of internal freedom related to the direction of the escaping secondary electron [23]. Based on a comparison of Eq. (14) with Eq. (3) or Eq. (2), it appears that the coherent approximation might underestimate the delocalization of inelastic scattering.

If we take an opposite extreme and assume a completely incoherent summation of intensities, Eq. (5) is replaced by:

$$\text{PSF}(r) \propto \text{FT}(dI/d\Omega) \quad (30)$$

With no cutoff to the Lorentzian angular distribution, the analytical solution is [34]:

$$\text{PSF}(r) \propto \text{FT}[(\theta^2 + \theta_E^2)^{-1}] = K_0(\theta_E k_0 r) \quad (31)$$

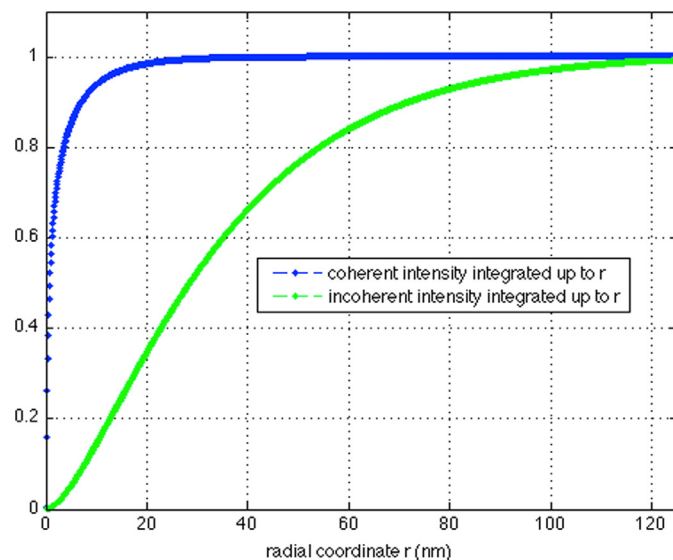


Fig. 14. Fraction of inelastic intensity within a radius r , calculated using Eq. (31) (green curve, incoherent approximation) and Eq. (17) (blue curve, coherent approximation), for $E = 6$ eV and $E_0 = 60$ keV. (For interpretation of the references to color in this figure legend, the reader is referred to the web version of this article.)

where K_0 is the same Bessel function as used in Eq. (21) but without a factor of 2 within the argument. As seen in Fig. 14, Eq. (34) predicts much more extensive delocalization than Eq. (17); the diameter d_{50} (containing 50% of the scattered electrons) is around 1000 nm for $E = 0.2$ eV, decreasing to 10 nm at $E = 25$ eV, values an order of magnitude larger than the trend shown in Fig. 1. Numerical evaluation of Eq. (30) with a Bethe-ridge angular cutoff leads to the same conclusion: that incoherent addition would greatly overestimate the degree of delocalization.

An attractive feature of the coherent approximation is that it predicts an exponential falloff of intensity at around $b_{\max}/2$, as verified experimentally [7]. Whereas Eq. (31) leads to an r -integrated intensity that does not saturate until about $6b_{\max}$, meaning very broad delocalization.

There appears to be a direct correlation between inelastic delocalization and the lateral coherence length $L_c(E)$ involved in inelastic scattering. Kimoto and Matsui [60] measured $L_c(E)$ from the focus dependence of lattice-fringe contrast and found values similar to those given by Eq. (2), for E between 10 eV and 400 eV. Holographic measurements are also possible [61]. Schattschneider and Werner [62] have argued that inelastic scattering by plasmon excitation is highly coherent and that inelastic scattering in general has a large coherent component.

Certainly there is a need for experimental data to verify or refine the simple theory presented here. *Ab-initio* calculations of delocalization for valence-electron and vibrational losses, perhaps based on the approach of Ritchie and Howie (22), would also be valuable. Especially if it can be cast in analytical form, the resulting PSF could be used in place of Eq. (17) to predict the properties discussed here.

Our equations have assumed single inelastic scattering, which becomes a poor approximation when the specimen thickness approaches or exceeds the mean free path λ_i for the inelastic process being detected. The value of λ_i is of the order of 100 nm for valence-electron (plasmon) scattering but many micrometers for dipole-mode vibrational (optical-phonon) scattering.

We have also ignored the simultaneous presence of elastic scattering in the specimen, whose extent is described (inversely) by an elastic mean free path λ_e in the case of a non-crystalline material.

Low-loss spectra are typically recorded using a spectrometer entrance aperture whose collection semiangle β is large enough to include a major part of the inelastic scattering but small enough to exclude most of the elastic scattering. For electrons transmitted through a specimen of thickness t , the fraction that escape elastic scattering is $\exp(-t/\lambda_e)$ and the energy-loss signal is reduced (at the aperture) by this factor. For a thin specimen with roughly uniform composition and thickness, the elastic scattering should not significantly affect the delocalization properties of the inelastic scattering. In a thicker specimen, plural elastic scattering can lead to “beam spreading” or “beam broadening” that degrades the spatial resolution of analysis and for which formulas are available [35]. Since this effect is uncorrelated with the inelastic scattering, it could be combined in quadrature with the delocalization length.

In calculating the PSF for energy deposition, we ignored the contribution from inner-shell excitation, which increases the average energy loss. The PSF for damage would then be narrower and perhaps comparable to the light-blue curve in Fig. 10. Inner-shell contributions will be important for higher specimens of medium or high atomic number.

10. Conclusions

We have discussed the delocalization of inelastic scattering in terms of a point spread function (sometimes called an object function), calculated as a square of the Fourier transform of the inelastic amplitude as a function of scattering angle (coherent approximation). The median delocalization distance L_{50} is a few nm for valence-electron losses in the range 5–30 eV and several tens of nm for vibrational-mode losses between 0.1 and 0.5 eV, in general agreement with experiment. This PSF can be approximated as a Lorentzian function with an exponential cutoff around the Bohr adiabatic limit, allowing easy calculation of the fraction of inelastic scattering occurring outside an electron probe of a given diameter.

By summing over energy losses between 5 eV and 100 eV, we calculated the radial distribution of energy deposition created by a sub-nm STEM probe in an organic specimen. This distribution can be interpreted as a PSF for radiolysis damage; its width is approximately 4 nm.

Combining the PSFs for signal and radiolysis leads to a quantitative explanation of previous EELS data recorded from several polymers. For probe diameters below 100 nm, the rate of double-bond scission depends on the probe current rather than current density.

According to our formulas, a coarse “leapfrog” scan provides an energy-loss signal that persists for longer than with regular scanning. But the time-integrated signal remains less, for the same spatial resolution.

Acknowledgments

This paper is dedicated to Dr. Ondrej Krivanek in recognition of his contributions to EELS instrumentation, which have greatly increased the power and convenience of the technique. During manuscript preparation, I benefited from the insightful comments of Chris Rossouw and Peter Crozier. I am grateful to the Natural Sciences and Engineering Research Council of Canada for continuing financial support.

References

- [1] O.L. Krivanek, T.C. Lovejoy, N. Dellby, T. Aoki, R.W. Carpenter, P. Rez, E. Soignard, J. Zhu, P.E. Batson, M.J. Lagos, R.F. Egerton, P.A. Crozier, *Nature* 514 (2014) 209.
- [2] P. Rez, T. Aoki, K. March, D. Gur, O.L. Krivanek, N. Dellby, T.C. Lovejoy, S.G. Wolf, H. Cohen, *Nat. Commun.* 7 (2015) 10945.
- [3] R.F. Egerton, *Ultramicroscopy* 159 (2015) 95.
- [4] M. Isaacson, J.P. Langmore, H. Rose, *Optik* 41 (1974) 92.
- [5] L.D. Marks, *Sol. State Commun.* 43 (1982) 727.
- [6] P.E. Batson, *Surf. Sci.* 156 (1985) 720.
- [7] D.A. Muller, J. Silcox, *Ultramicroscopy* 59 (1995) 195.
- [8] W. Zhou, S.J. Pennycook, J.-C. Idrobo, *Ultramicroscopy* 12 (2012) 51.
- [9] K. van Benthem, R.H. French, W. Sigle, C. Elsasser, M. Rühle, *Ultramicroscopy* 86 (2001) 303.
- [10] A.B. Shah, Q.M. Ramasse, J.G. Wen, A. Bhattacharya, J.N. Eckstein, J.M. Zuo, *Micron* 42 (2011) 539.
- [11] K.M. Adamson-Sharpe, F.P. Ottensmeyer, *J. Microsc.* 122 (1981) 309.
- [12] H. Shuman, C.-F. Chang, A.P. Somlyo, *Ultramicroscopy* 19 (1986) 121.
- [13] C. Mory, H. Kohl, M. Tence, C. Colliex, *Ultramicroscopy* 37 (1991) 191.
- [14] J.C.H. Spence, J. Taftø, *J. Microsc.* 130 (1983) 147.
- [15] J. Taftø, O.L. Krivanek, *Phys. Rev. Lett.* 48 (1982) 560.
- [16] A.J. Bourdillon, *Philos. Mag.* 50 (1984) 839.
- [17] S.J. Pennycook, *Ultramicroscopy* 26 (1988) 239 *Contemp. Phys.* 23 (1982) 371.
- [18] C.J. Rossouw, P.S. Turner, T.J. White, A.J. O'Connor, *Philos. Mag. Lett.* 60 (1989) 225.
- [19] W. Qian, B. Totdal, R. Hoier, J.C.H. Spence, *Ultramicroscopy* 41 (1992) (1992) 147.
- [20] J.S. Jeong, M.L. Odlyzko, P. Xu, B. Jalan, K.A. Mkhoyan, *Phys. Rev. B* 93 (2016) 165140.
- [21] H. Rose, in: *Proceedings of the 31st Annual EMSA Meeting*, 1973, p. 286.
- [22] R.H. Ritchie, *Philos. Mag.* 44 (1981) 931 R.H. Ritchie, A. Howie, *Philos. Mag.* 58 (1988) 753.
- [23] V.W. Maslen, C.J. Rossouw, *Philos. Mag.* 47 (1983) 119; C.J. Rossouw, V.M. Maslen, *Philos. Mag.* 49 (1984) 743.
- [24] H. Kohl, H. Rose, *Adv. Electron. Electron Phys.* 65 (1985) 175.
- [25] M. Schenner, P. Schattschneider, *Ultramicroscopy* 55 (1994) 31.
- [26] D. Muller, J. Silcox, *Ultramicroscopy* 59 (1995) 195.
- [27] M.P. Oxley, L.J. Allen, *Acta Crystallographica A* 56 (2000) 470.
- [28] P. Schattschneider, M. Nelhiebel, H. Souchay, M. Jouffrey, *Micron* 31 (2000) 333.
- [29] E.C. Cosgriff, M.P. Oxley, L.J. Allen, S.J. Pennycook, *Ultramicroscopy* 102 (2005) 317.
- [30] H.L. Xin, L.F. Kourkoutis, J.A. Mundy, H. Zheng, D.A. Muller, *Microsc. Microanal.* 16 (Suppl. 2), p.242, doi:10.1017/S1431927610061623.
- [31] R.G. Wilson, *Fourier Series and Optical Transform Techniques in Contemporary Optics*, Wiley, New York, 1995 Chapter 6.
- [32] J.C.H. Spence, *High-Resolution Electron Microscopy*, 4th ed., Oxford University Press, 2013.
- [33] L. Reimer, H. Kohl, *Transmission Electron Microscopy*, 5th ed., Springer, 2008.
- [34] E.J. Burr, *Aust. J. Phys.* 8 (1955) 46.
- [35] R.F. Egerton, *Electron Energy-Loss Spectroscopy in the Electron Microscope*, 3rd ed., Springer, 2011.
- [36] A. Howie, R.H. Milne, *Ultramicroscopy* 18 (1985) 427.
- [37] Z.L. Wang, *Micron* 27 (1996) 265.
- [38] F.J. Garcia de Abajo, *Rev. Mod. Phys.* 82 (2010) 209.
- [39] L.W. Hobbs, *Introduction to Analytical Electron Microscopy*, in: J.J. Hren, J.I. Goldstein, D.C. Joy (Eds.), Plenum Press, New York, 1979 Chapter 17.
- [40] R.F. Egerton, *Microsc. Res. Tech.* 75 (2012) 1550.
- [41] K. Varlot, J.M. Martin, C. Quet, Y. Kihn, *Ultramicroscopy* 68 (1997) 123.
- [42] K. Siangchaew, M. Libera, *Philos. Mag. A* 80 (2000) 1001.
- [43] R.F. Egerton, S. Lazar, M. Libera, *Micron* 43 (2012) 2.
- [44] B. Wu, A.R. Neureuther, *Energy deposition and transfer in electron-beam lithography*, *J. Vac. Sci. Technol. B* 19 (2001) 2508–2511.
- [45] R.F. Egerton, P. Li, M. Malac, *The lateral range and energy deposition of fast secondary electrons*, *Microsc. Microanal.* 10 (Suppl. 2) (2004) 1382CD–1383CD, doi:10.1017/S1431927604880541.
- [46] G. Han, F. Cerina, *Energy transfer between electrons and photoresist: its relation to resolution*, *J. Vac. Sci. Technol. B* 18 (2000) 3297–3302.
- [47] A. Howie Echenique, R.H. Ritchie, *Phys. Rev. Lett.* 83 (1999) 658.
- [48] H. Cohen, T. Maniv, R. Tenne, Y. Rosenfeld Hakohen, O. Stephan, C. Colliex, *Phys. Rev. Lett.* 80 (1998) 782 83 (1999) 659.
- [49] R.F. Egerton, T. Aoki, P.A. Crozier, *Microsc. Microanal.* 22 (Suppl. 3) (2016), doi:10.1017/S1431927604880541.
- [50] P. Rez, *Personal communication* (2016).
- [51] M. Inokuti, *Rev. Mod. Phys.* 43 (1971) 297.
- [52] H. Ibach, *Physics of Surfaces and Interfaces*, Springer-Verlag, Berlin, 2006 IS-BN-13 978-3-540- 34709-5.
- [53] W. Ho, R.F. Willis, E.W. Plummer, *Phys. Rev. Lett.* 40 (1978) 1729.
- [54] R.F. Willis, *Vibrational Spectroscopy of Adsorbates*, in: R.F. Willis (Ed.), Springer Verlag, 1980 Ch. 1 and Ch.4.
- [55] P. Rez, *Microsc. Microanal.* 20 (2014) 671.
- [56] C. Dwyer, *Phys. Rev. B* 89 (2014) 054103.
- [57] P. Cueva, D.A. Muller, *Microsc. Microanal.* 20 (Suppl. 3) (2014) S590.
- [58] N.R. Lugg, B.D. Forbes, S.D. Findlay, L.J. Allen, *Phys. Rev. B* 91 (2015) 144108.
- [59] C. Dwyer, T. Aoki, P. Rez, S.L.Y. Chang, T.C. Lovejoy, O.L. Krivanek, *Phys. Rev. Lett.* 117 (2016) 256101.
- [60] K. Kimoto, Y. Matsui, *Ultramicroscopy* 96 (2003) 335.
- [61] R.A. Herring, *J. Electron Microsc.* 58 (2009) 213.
- [62] P. Schattschneider, W.S.M. Werner, *J. Electron Spectrosc.* 143 (2005) 81.